INORGANIC CHEMISTRY FRONTIERS

RESEARCH ARTICLE

View Article Online
View Journal | View Issue

Cite this: *Inorg. Chem. Front.*, 2026, **13**, 3628

Layered perovskite-like nitrates $A_2Ca(NO_3)_2Cl_2$ (A = Rb, Cs) as ultraviolet birefringent optical materials

Hussin Elkik,[a,b,c] Muhammad Mujahid Iqbal,[a,b] Aqsa Munawar,[a,b] Zhihua Yang,[a,b] Fangfang Zhang *[a,b] and Shilie Pan *[a,b]

Received 13th January 2026,
Accepted 24th February 2026

DOI: 10.1039/d6qi00086j

rsc.li/frontiers-inorganic

The progress of all-inorganic Ruddlesden–Popper (RP) perovskites broadens the selection of materials suitable for optoelectronic applications, especially in improving stability and performance. Two new alkali metal calcium halide nitrate-based layered RP perovskite variants, $Rb_2Ca(NO_3)_2Cl_2$ and $Cs_2Ca(NO_3)_2Cl_2$, have been synthesized through a facile solution evaporation method. Remarkably, the title compounds exhibit a unique RP perovskite-like nitrate layered structure with significant birefringence (0.099–0.104@546 nm) and short ultraviolet (UV) absorption wavelengths (220–225 nm). In-depth structural investigation and theoretical analyses indicate that the birefringence substantially arises from the planar triangular $[NO_3]$ groups. This study not only enhances the structural diversity of layered perovskites but also provides an effective strategy for the continued investigation of all-inorganic birefringent optical materials in the UV region.

Introduction

Ultraviolet (UV) birefringent crystals are becoming increasingly significant in modern technology and scientific applications, such as polarimetry, optical communication, and scientific instrumentation.[1,2] Owing to their remarkable ability to modify light polarization, birefringent materials have garnered significant interest as important optical materials.[3–5] Numerous UV birefringent crystals, including $CaCO_3$,[6] MgF_2,[7] and α-BBO,[8] have been developed and commercialized over the past few decades. Though the drawbacks related to these materials, such as the contaminants and crystal growth challenges of $CaCO_3$, the limited birefringence of MgF_2, and the crystal growth crack caused by phase transformation for α-BBO, have severely restricted their practical applications. Therefore, it is critical to create efficient plans for discovering new, high-performing UV birefringent materials.

A metal cation polyhedron in an extremely deformed structure is advantageous for the formation of large polarizability anisotropy, leading to a notable increase in birefringence:[9] as an illustration, consider $K_2SbMoO_2F_7$,[10] an ordered d^0 transition metal fluoroantimonite with a significant birefringence of 0.220@550 nm or a metal cation deformed polyhedron, such as PbO_4Br_4 in $Cs_2Pb(NO_3)_2Br_2$ [5] (Δn = 0.147@546 nm) and SnO_7Cl_2 in $Sn_2B_5O_9Cl$ [11] (Δn = 0.168@546 nm), caused by the action of stereochemically active lone pairs (SCALP).[12–17] Unfortunately, the incorporation of SCALP metal cations or d^0 transition metal cations leads to a significant red shift in the UV cutoff edge, rendering this method unsuitable for exploring new good birefringent materials in the UV range. As a result, alkali metals and alkaline-earth metals are typically selected to develop novel UV optical materials, achieving high transmittance in the UV range. Consequently, the advancement of innovative UV birefringent crystals will critically depend on how to effectively employ the anionic groups to optimize their birefringence contribution.

In the context of anion frameworks, achieving high birefringence is favored by two key factors: (1) anionic groups with large anisotropy, such as planar groups, $[BO_3]$, $[NO_3]$, $[CO_3]$, and $[C_3N_3O_3]$,[18–29] and (2) their arrangement, particularly when these planar units are organized in a layered structure. This is attributed to the optimized alignment of microscopic polarizability anisotropy. A prominent class of layered materials with anisotropic anionic groups is the family of layered perovskites ($A_{n+1}B_nX_{3n+1}$; where X = Cl^-, NO_3^-).[30–34] For example, in $Cs_2Pb(NO_3)_2Cl_2$ [35] and $Cs_2Pb(NO_3)_2Br_2$,[5] the layered arrangement of π-conjugated $[NO_3]^-$ anion groups and SCALP-active Pb^{2+} cations exert a synergistic effect to enhance the material's birefringence. Herein, we proposed to strategically replace Pb^{2+} with Ca^{2+} for the targeted design and development of new birefringent materials effective in the shorter

[a]*Research Center for Crystal Materials, CAS Key Laboratory of Functional Materials and Devices for Special Environmental Conditions, Xinjiang Key Laboratory of Functional Crystal Materials, Xinjiang Technical Institute of Physics and Chemistry, Chinese Academy of Sciences, 40-1 South Beijing Road, Urumqi 830011, China. E-mail: ffzhang@ms.xjb.ac.cn, slpan@ms.xjb.ac.cn*

[b]*Center of Materials Science and Optoelectronics Engineering, University of Chinese Academy of Sciences, Beijing 100049, China*

[c]*Department of Chemistry, Faculty of Science, Qena University, Qena 83523, Egypt*

UV range. Additionally, Rb and Cs cations were chosen as counter ions to ensure charge equilibrium.

Two new alkali metal calcium halide nitrates, $A_2Ca(NO_3)_2Cl_2$, (A = Rb, Cs), were successfully obtained. Notably, both compounds exhibit a unique layered structure composed of consecutive two-dimensional (2D) perovskite slabs that resemble Ruddlesden–Popper perovskite,[35] $[Ca(NO_3)_2Cl_2]^{2-}_{\infty}$ anion layers, and interlayer Rb^+ and Cs^+ cations. This structure endows them with excellent multifunctional optical properties, including considerable birefringence values and short UV absorption wavelengths.

Experimental

Reagents and crystal growth

All starting materials were utilized without additional purification: $CsNO_3$ (AR 99.5%, Macklin Chemicals), RbCl (AR 99.5%, Macklin Chemicals), $Ca(NO_3)_2{\cdot}4H_2O$ (AR 99.5%, Aladdin Chemicals) and $CaCl_2$ (AR 99.9%, Aladdin Chemicals). Single crystals of $A_2Ca(NO_3)_2Cl_2$ (A = Rb, Cs) were prepared *via* a room-temperature water evaporation method. Reagents were weighted as follows: for $Rb_2Ca(NO_3)_2Cl_2$, RbCl (0.605 g, 5 mmol) and $Ca(NO_3)_2{\cdot}4H_2O$ (1.181 g, 5 mmol); for $Cs_2Ca(NO_3)_2Cl_2$, $CsNO_3$ (0.975 g, 5 mmol) and $CaCl_2$ (0.555 g, 5 mmol). The weighed samples were placed in 100 mL beakers, respectively, and each beaker was filled with 20 mL of water. The measured pH values of the aqueous solutions were found to be in the range of 5–7. The opening of each beaker was covered with a stretch film punctured with a few holes to allow a very slow water evaporation rate in the air. Eventually, colourless bulk crystals (Fig. S1) were obtained with yields of 60–70% (based on Ca). Transparent, high-quality single crystals of $A_2Ca(NO_3)_2Cl_2$ (A = Rb, Cs) were carefully selected under an optical microscope for further structural characterization. Polycrystalline powder samples for characterization were prepared by grinding the bulk crystals.

Single-crystal X-ray diffraction

Single-crystal X-ray diffraction analysis was conducted with a Bruker SMART APEX II CCD diffractometer, utilizing a Mo Kα radiation source with λ = 0.71073 Å.[36] The collected data were subsequently processed with SAINT software. After data collection and integration, the crystal structures were solved and refined using direct methods from SHELXTL software suite.[37] The full-matrix least-squares refinement provided accurate atomic coordinates for all atoms in the structures. The PLATON program and the CIF check tool (**https://checkcif.iucr.org**) were used to verify the crystal structures.[38] Table 1 presents the structural refinement data for both crystals.

Elemental analysis

Elemental composition of the samples was determined using energy-dispersive X-ray spectroscopy (EDS) integrated with a JEOL JSM-7610F Plus field-emission scanning electron microscope (FE-SEM) operating at an accelerating voltage of 5 kV.

Table 1 Refined structure and crystallographic data for $Rb_2CaN_2O_6Cl_2$ and $Cs_2CaN_2O_6Cl_2$

Molecular formula	$Rb_2CaN_2O_6Cl_2$	$Cs_2CaN_2O_6Cl_2$
Formula weight	405.94	500.82
Temperature/K	298.0	298.0
Radiation	Mo Kα, λ = 0.71073 Å	Mo Kα, λ = 0.71073 Å
Crystal system, space group	Tetragonal, $I4_1/amd$	Tetragonal, $I4_1/amd$
a (Å)	5.4268(2)	5.5603(5)
b (Å)	5.4268(2)	5.5603(5)
c (Å)	31.877(2)	32.482(3)
β (Å)	90	90
Volume (Å^3)	938.77(9)	1004.2(2)
Z	4	4
$\rho_{calc.}$ (g cm^{-3})	2.872	3.313
Index ranges	$-7 \le h \le 7$, $-6 \le k \le 7$, $-40 \le l \le 39$	$-7 \le h \le 7$, $-7 \le k \le 7$, $-39 \le l \le 39$
μ (mm^{-1})	11.539	8.301
F (000)	760.0	904.0
2θ range	5.112 to 54.974	5.016 to 54.954
Collected reflections	7509	3343
Independent reflections	328 [R_{int} = 0.0506]	335 [R_{int} = 0.0591]
Completeness (%)	100	96
Goodness-of-fit on F^2	1.063	1.232
Final R indices [$I > 2$sigma(I)][a]	R_1 = 0.0147, wR_2 = 0.0354	R_1 = 0.0238, wR_2 = 0.0507
Data/restraints/parameters	328/0/26	335/0/26

[a] $F_o^2 > 2\sigma(F_o^2)$, $R_1 = \sum||F_o| - |F_c||/\sum|F_o|$ and $wR_2 = [\sum w(F_o^2 - F_c^2)^2/\sum wF_o^4]^{1/2}$.

Powder X-ray diffraction

Powder X-ray diffraction (PXRD) analysis was completed utilizing Cu Kα (λ = 1.54056 Å) radiation on a Bruker D2 PHASER diffractometer. The experiment was conducted at ambient temperature with a 2θ angle range of 5–70°, using a scan step width of 0.01° and a fixed duration of 0.2 s.

Optical characteristics

IR spectra of $Rb_2Ca(NO_3)_2Cl_2$ and $Cs_2Ca(NO_3)_2Cl_2$ were tested using a Shimadzu IR Affinity-1 Fourier transform infrared spectrometer at a resolution of 1 cm^{-1}, over a spectral range of 400–4000 cm^{-1} and utilizing a KBr disc as a reference (1 : 100 as sample : KBr ratio). The UV-vis-NIR transmittance spectra were recorded at room temperature using a Shimadzu SolidSpec-3700DUV spectrophotometer and polished crystal wafers (≈0.3 mm thick) over the spectral window of 200–1600 nm. UV-vis-NIR diffuse reflection data were further collected. The measurements extended across wavelengths from 200 nm to 2600 nm. The Kubelka–Munk function, $K/S = (1 - R)^2/2R$, was used to extract absorption data from diffuse reflection data. K and S stand for the absorption and scattering coefficients, respectively.[39–42] By extending the absorption edge to the baseline on the K/S *versus* energy plot, the band gap value can be determined.

Thermal analysis

To assess the thermal stability of the compounds, we conducted concurrent differential scanning calorimetry and

thermogravimetric analysis using a Netzsch STA 449 F3 analyzer. A controlled heating program at a rate of 5 °C min^{-1} was utilized to evaluate the thermal stability of $A_2Ca(NO_3)_2Cl_2$ (A = Rb, Cs) in powder form. Each sample was seated inside an alumina crucible and subjected to a controlled heating procedure from ambient temperature (25 °C) to 1000 °C.

Refractive index difference measurements

The birefringence of $Rb_2Ca(NO_3)_2Cl_2$ and $Cs_2Ca(NO_3)_2Cl_2$ was measured using a cross-polarizing microscope (ZEISS Axio Scope. 5) equipped with a Berek compensator. The wavelength of the light source is 546 nm. The relative error was minimized due to the clear visibility of the first-, second-, and third-order interference color boundaries. To enhance the accuracy of the birefringence measurements, small, transparent single crystals of $Rb_2Ca(NO_3)_2Cl_2$ and $Cs_2Ca(NO_3)_2Cl_2$ were utilized. The birefringence (Δn) was calculated using the formula: $R = |N_g - N_p| \times T = \Delta n \times T$, where R represents the difference in the optical path, N_g and N_p are the refractive indices of fast and slow light, and T is the thickness of the crystal sample.[43]

Theoretical calculations

The electronic structure calculations were carried out by first-principles methods with the CASTEP package, employing norm-conserving pseudopotentials (NCPs).[44] The exchange–correlation potential was described using the Perdew–Burke–Ernzerhof (PBE) functional, a representative of the generalized gradient approximation (GGA).[45] The following valence electron configurations were considered for the norm-conserving pseudopotentials: Rb-$4s^24p^65s^1$; Cs-$5s^25p^66s^1$; Ca-$3s^23p^64s^2$; N-$2s^22p^3$; Cl-$3s^23p^5$; O-$2s^22p^4$. The kinetic energy cutoff for the plane-wave basis was set to 750 eV for both $Rb_2Ca(NO_3)_2Cl_2$ and $Cs_2Ca(NO_3)_2Cl_2$.[46] The Brillouin zone was sampled using Monkhorst–Pack k-point meshes of 5 × 5 × 1 and 6 × 6 × 1 for $Rb_2Ca(NO_3)_2Cl_2$ and $Cs_2Ca(NO_3)_2Cl_2$, respectively. Owing to the inherent discontinuity in the exchange–correlation energy, the band gaps calculated with GGA-PBE are generally underestimated. To align the calculated band gaps with the experimentally measured values, a scissor operator was applied to rigidly shift all conduction bands upward.

Results and discussion

Crystal structure

$A_2Ca(NO_3)_2Cl_2$ (A = Rb, Cs) crystallize in the tetragonal space group $I4_1/amd$ (no. 141). As $A_2Ca(NO_3)_2Cl_2$ (A = Rb, Cs) are isostructural, the structure of $Cs_2Ca(NO_3)_2Cl_2$ is presented in detail as a representative example. The asymmetric unit has one independent Cs, one Ca, one Cl, one N, and two O atoms. According to Fig. 1, the structure consists of CaO_4Cl_4 polyhedra and [NO_3] trigonal planar groups. A CaO_4Cl_4 polyhedron with Ca–Cl and Ca–O bond lengths of 2.801(4) and 2.582(4) Å, respectively, is formed when the Ca atom coordinates with four Cl and four O atoms (Fig. 1a). Cl–Ca–Cl and O–Ca–O bond angles are 90.845(8)–166.05(7)° and 48.90(18)–145.97

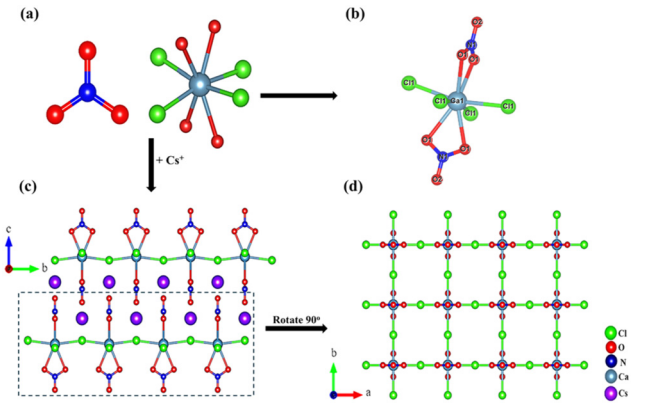

Fig. 1 (a) Ball-and-stick models depicting the [NO_3] unit and the CaO_4Cl_4 polyhedron. (b) Crystal structure of $[Ca(NO_3)_2Cl_2]^{2-}$; observe that the two *trans* [NO_3] groups are aligned perpendicularly to one another. (c) The *bc*-plane view of the crystal structure of $Cs_2Ca(NO_3)_2Cl_2$. (d) A single $[Ca(NO_3)_2Cl_2]^{2-}_{\infty}$ layer consisting of NO_3 groups and CaO_4Cl_4 polyhedra, as seen in the *ab*-plane.

(12)°, respectively. Through two apical bidentate nitrate groups with N–O bond lengths of 1.227–1.257 Å, the CaO_4Cl_4 polyhedron shares four oxygen atoms. What's interesting to note is that the two *trans* [NO_3] groups positioned at right angles to one another are coordinated to the calcium central atom (Fig. 1b). Compared to the uncoordinated N–O bond length (1.227(8) Å), the two bond lengths of N–O utilized for the Ca^{2+} coordination are comparatively longer (1.257(5) Å). Adjacent eight-coordinate distorted CaO_4Cl_4 polyhedra form a 2D $[Ca(NO_3)_2Cl_2]_{\infty}^{2-}$ anion layer in the *ab*-plane (Fig. 1d) by sharing Cl atoms in the equatorial plane, with Cs^+ cations positioned between the layers to maintain charge balance (Fig. 1c). The layer shows eight-membered square rings (Fig. 1d). The square rings have approximate dimensions of 5.560(6) Å × 5.560(6) Å. The special Cs^+ cation is in 12-fold coordination geometry with eight Cs–O connections that range from 3.164(3) to 3.807 (4) Å and four Cs–Cl links that range from 3.442(11) to 3.882 (13) Å. Moreover, we examined the angular variations between the $Cs_3Ca_2Cl_7$ [47] and $Cs_2Ca(NO_3)_2Cl_2$ structures. All the Cl–Ca–Cl angles are nearly 90°, as seen in panels a and b of Fig. S4a and b, leading to the almost flat layers made up of $CaCl_4$ squares for $Cs_3Ca_2Cl_7$. Nevertheless, the N–Ca–Cl angles in $Cs_2Ca(NO_3)_2Cl_2$ (Fig. S4c and d) are 96.97 and 83.03°, respectively, indicating that the $CaCl_4$ square layers are corrugated because of the steric barrier effect of the mutually perpendicular [NO_3] groups. Therefore, the degree of deformation of the Ca-centred polyhedron is significantly increased when the [NO_3] groups replace the apical halogen atoms.

The structural similarity of $Cs_2Ca(NO_3)_2Cl_2$ to layered perovskites ($A_{n+1}B_nO_{3n+1}$) is one of its most intriguing structural characteristics. Layered perovskites, in general, consist of endless 2D ABO_3-type structural layers separated by a motif. One of the main families of layered perovskites that has been categorized according to the motif that divides the layers, and their offsetting methods, is Ruddlesden–Popper (RP) com-

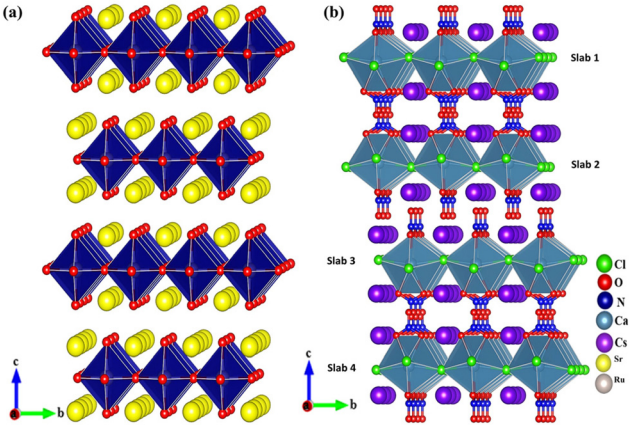

Fig. 2 (a) The polyhedral depiction of the Ruddlesden–Popper layered perovskite with n = 1, specifically Sr_2RuO_4. The structure is composed of infinite layers of RuO_6 octahedra that share corners. Sr^{2+} cations completely occupy the interlayer sites. (b) Polyhedral depiction of $Cs_2CaCl_2(NO_3)_2$ highlights the offset of the slabs in the *bc*-plane due to the coordinated $[NO_3]^-$ units. Cs^+ cations separate the corner-sharing CaO_4Cl_4 polyhedra's 2D layers with apical $[NO_3]^-$ ligands.

pounds. Fig. 2a shows a typical structure of the n = 1 Ruddlesden–Popper family, Sr_2RuO_4.[48] The corner-sharing RuO_6 octahedra produce endless 2D slabs that are separated by Sr cations. Furthermore, a (1/2, 1/2) translation is applied to the layers in the [100] and [010] directions to offset them. On the other hand, slabs of corner-shared CaO_4Cl_4 polyhedra are exhibited by $Cs_2Ca(NO_3)_2Cl_2$ through chlorine atoms, and the Cs^+ cations are located at interlayer sites (Fig. 2b). The $Cs_2Ca(NO_3)_2Cl_2$ and the n = 1 layered perovskites share a similar structural motif, despite the B site having an 8-coordination. Furthermore, as can be shown in Fig. 2b, the CaO_4Cl_4 polyhedra include $[NO_3]^-$ apical ligands, which are rarely seen in any perovskite family. A closer glance at the structure exhibits that the coordinated $[NO_3]^-$ ligands are crucial for the offset of the layers in $Cs_2Ca(NO_3)_2Cl_2$. The offset between slabs 2 and 3 corresponds to a 1/2 translation along the [100] direction (Fig. 2b). However, no offset along [100] was observed between slabs 1 and 2, or between slabs 3 and 4. Nevertheless, between slabs 1 and 2 or 3 and 4, there are offsets corresponding to a 1/2 translation in the [010] direction. The reason behind all these offsets appears to be the planar $[NO_3]^-$ groups that are coordinated perpendicularly to avoid the layers making undesirable direct interactions. Therefore, by fitting slabs 1 and 2 (or slabs 3 and 4) with the $[NO_3]^-$ "studs" aligned along the *a*-direction and then further interlocking those fitted double slabs in the *b*-direction, the framework structure of $Cs_2Ca(NO_3)_2Cl_2$ can be constructed.

The calculated values of bond valence sums (BVS) of $Cs_2Ca(NO_3)_2Cl$ 1.166, 2.007, 1.073, 2.006–2.020 and 4.950 are in accordance with the oxidation states of Cs^+, Ca^{2+}, Cl^-, O^{2-} and N^{5+}, respectively (Table S4). Elemental analysis using energy dispersive X-ray spectroscopy (EDS) was conducted, as depicted in Fig. S6. The ratios of Ca : Rb : Cl and Ca : Cs : Cl were found to be approximately, 1.00 : 1.98 : 1.85 and 1.00 : 2.29 : 1.84, respectively, which align with the single-crystal structure analysis for $Rb_2Ca(NO_3)_2Cl_2$ and $Cs_2Ca(NO_3)_2Cl_2$.

Phase analysis

The PXRD patterns for $Rb_2Ca(NO_3)_2Cl_2$ and $Cs_2Ca(NO_3)_2Cl_2$ match well with the XRD patterns that were computed using the single-crystal models (Fig. 3a and d). The matching of the XRD patterns confirms that the samples are adequately pure for the subsequent performance tests.

Thermal analysis

The differential scanning calorimetry (DSC) and thermogravimetric analysis (TGA) curves indicate that $Rb_2Ca(NO_3)_2Cl_2$ and $Cs_2Ca(NO_3)_2Cl_2$ can remain stable up to approximately 490–525 °C, suggesting that both compounds exhibit high thermodynamic stability. The DSC curves show endothermic peaks at around 302 °C and 296 °C, corresponding to the melting points of $Rb_2Ca(NO_3)_2Cl_2$ and $Cs_2Ca(NO_3)_2Cl_2$, respectively. The TG curves for the title compounds exhibit two steps of weight loss for $Rb_2Ca(NO_3)_2Cl_2$ (Fig. 3b). The first step occurs between 490 and 625 °C, featuring a weight loss of 25.70%, attributed to the evaporation of one N_2O_5 (calculated value: 26.61%). The second step, occurring from 625 to 850 °C, relates to the decomposition of one Rb_2O and one Cl_2, resulting in a weight loss of 61.80% (calculated value: 63.51%). On the other hand, $Cs_2Ca(NO_3)_2Cl_2$ (Fig. 3e) exhibits a single weight loss step between 525 and 970 °C, with a weight loss of 88.50% (calculated value: 92.00%) due to the evaporation of one N_2O_5, one Cl_2, and one Cs_2O.

Optical properties

As shown in Fig. S5a and b, the infrared spectra of $Rb_2Ca(NO_3)_2Cl_2$ and $Cs_2Ca(NO_3)_2Cl_2$ indicate that the bands at 1431, 1380, and 1045 cm^{-1}, along with those at 1465, 1384, and 1044 cm^{-1}, correspond to N–O stretching vibrations in the $[NO_3]$ triangles. Additionally, the bands at 825 and 730 cm^{-1} for $Rb_2Ca(NO_3)_2Cl_2$ and 822 and 727 cm^{-1} for $Cs_2Ca(NO_3)_2Cl_2$ are attributed to the nonplanar bending vibrations of the $[NO_3]$ planar groups. These findings are consistent with previously published studies.[49–51] The UV-vis-NIR transmittance spectra of $Rb_2Ca(NO_3)_2Cl_2$ and $Cs_2Ca(NO_3)_2Cl_2$ reveal that the preliminarily polished single-crystal plates exhibit short UV cutoff edges at 225 and 220 nm, corresponding to band gaps of 5.51 eV and 5.64 eV, respectively (Fig. 3c and f). In addition, diffuse reflectance spectra of $Rb_2Ca(NO_3)_2Cl_2$ and $Cs_2Ca(NO_3)_2Cl_2$ have been studied (Fig. S5c and d). The overall band gaps of the materials may be related to the extent of distortions associated with the CaO_4Cl_4 polyhedra. These large band gap values are notably higher than those of $Cs_2Pb(NO_3)_2Cl_2$ and $Cs_2Pb(NO_3)_2Br_2$ (3.5 and 3.01 eV) due to the incorporation of calcium atoms with no d–d or f–f transitions, implying that our title compounds may have potential applications as short UV birefringent materials. The birefringence of $A_2Ca(NO_3)_2Cl_2$ (A = Rb, Cs) was evaluated using a cross-polarizing microscope (ZEISS Axio Scope. 5). $Rb_2Ca(NO_3)_2Cl_2$ and $Cs_2Ca(NO_3)_2Cl_2$

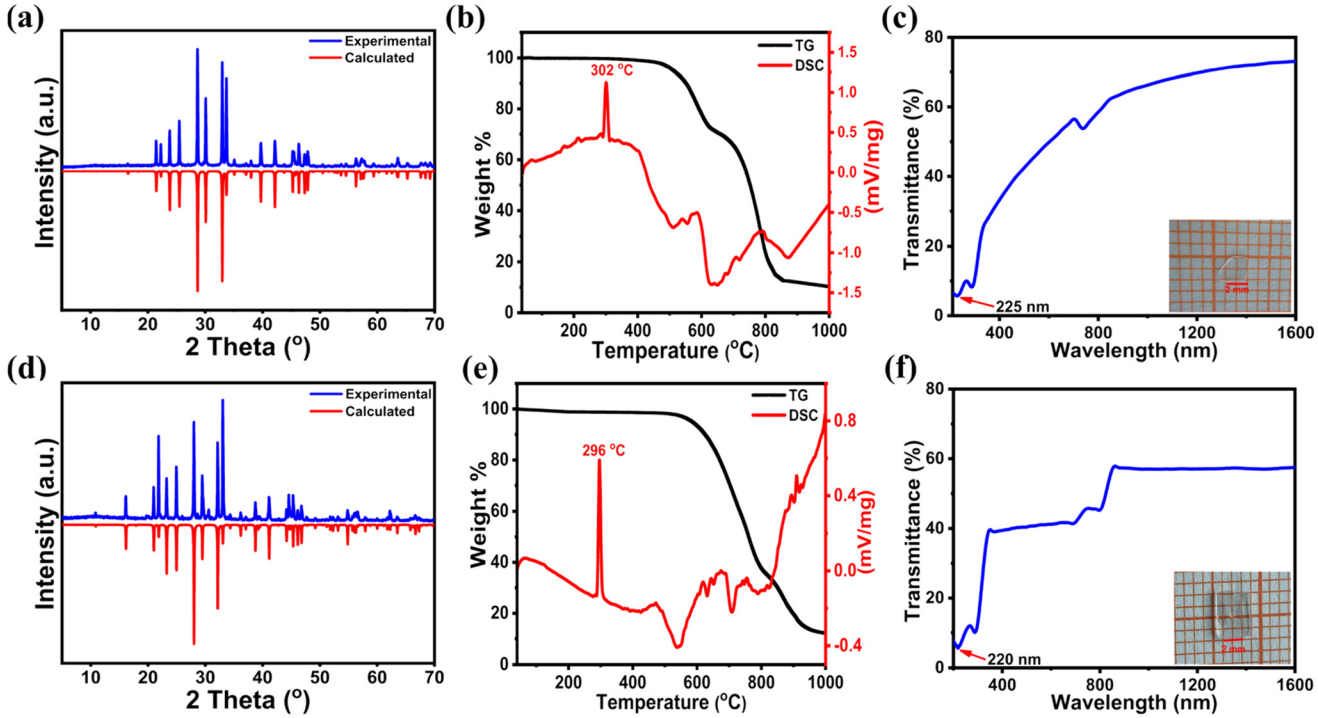

Fig. 3 Experimental and calculated powder X-ray diffraction patterns of $Rb_2Ca(NO_3)_2Cl_2$ (a) and $Cs_2Ca(NO_3)_2Cl_2$ (d). TG-DSC curves of $Rb_2Ca(NO_3)_2Cl_2$ (b) and $Cs_2Ca(NO_3)_2Cl_2$ (e). UV-vis-NIR transmittance spectrum of $Rb_2Ca(NO_3)_2Cl_2$ (c) and $Cs_2Ca(NO_3)_2Cl_2$ (f). An inset shows a polished crystal approximately 1 mm thick, which was used for the transmittance measurement.

display significant birefringence values of 0.099 and 0.104@546 nm, respectively (Table S7 and Fig. 4). These values are comparable to those of the commercially available birefringent crystal, α-BBO with the birefringence of 0.122@546 nm,[8] and $KSrCO_3F$ with the birefringence of 0.112@532 nm.[52] It is widely recognized that the presence of a planar π-conjugated anionic group [NO_3] can significantly enhance birefringence.

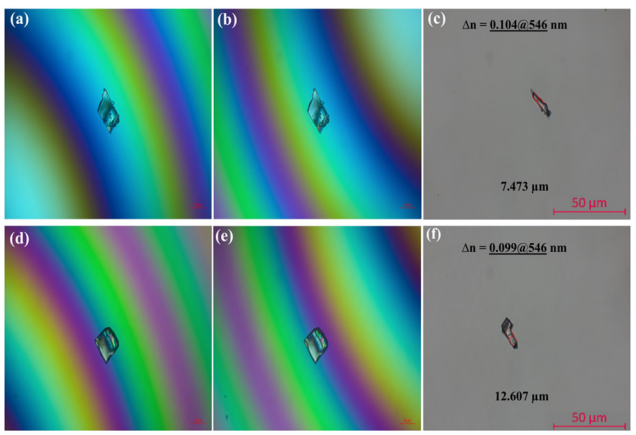

Fig. 4 Birefringence measurements of $Rb_2Ca(NO_3)_2Cl_2$ and $Cs_2Ca(NO_3)_2Cl_2$ using a polarizing microscope. Panels (a and b) and (d and e) display the views of the crystals at extinction during negative and positive rotations of the compensator for $Rb_2Ca(NO_3)_2Cl_2$ and $Cs_2Ca(NO_3)_2Cl_2$, respectively; panels (c) and (f) show the thickness of the crystals used for measurement.

When comparing our compounds to several reported nitrate compounds of alkali and alkaline earth metals, we observe that the birefringence values of our compounds are greater than those of $Ba_2B_5O_8(OH)_2(NO_3)(H_2O)_3$ (calculated, 0.033@1064 nm),[53] $Rb(NO_3)(SO_3NH_3)$ (experimental, 0.070@546 nm),[54] $Sr(NH_2SO_3)(NO_3)(H_2O)$ (experimental, 0.077@546.1 nm),[55] $Ba_2(OH)_3(NO_3)$ (experimental, 0.080@589.3 nm),[49] $KRb_2(NO_3)_2Cl$ (calculated, 0.084@1064 nm),[56] and $Na_3K_6(CO_3)(NO_3)_2(H_2O)_6$ (experimental, 0.094@546 nm).[57] However, the birefringence values for our compounds are lower than that of $Cs_2Pb(NO_3)_2Br_2$ (0.147@546 nm). Summary of some recently reported UV/visible halide, nitrate-halide-based, and hybrid perovskites is mentioned in Table S8.

Theoretical calculations

To acquire a deeper understanding of the relationship between microstructure and optical properties in $Rb_2Ca(NO_3)_2Cl_2$ and $Cs_2Ca(NO_3)_2Cl_2$, we employed systematic theoretical calculations using density functional theory (DFT).[45,58,59] As illustrated in Fig. 5a and e, calculations of band structures indicate that $Rb_2Ca(NO_3)_2Cl_2$ and $Cs_2Ca(NO_3)_2Cl_2$ possess indirect band gaps of 3.495 and 3.555 eV, respectively. The calculated values are lower than the experimental range (5.51–5.64 eV) due to the typical tendency of the DFT method to underestimate the band gap.[60,61] Consequently, a scissors operator was applied as the difference between the experimentally observed and the calculated GGA band gap.

The electron clouds at the top of the valence band (VB) and the bottom of the conduction band (CB), which are close to

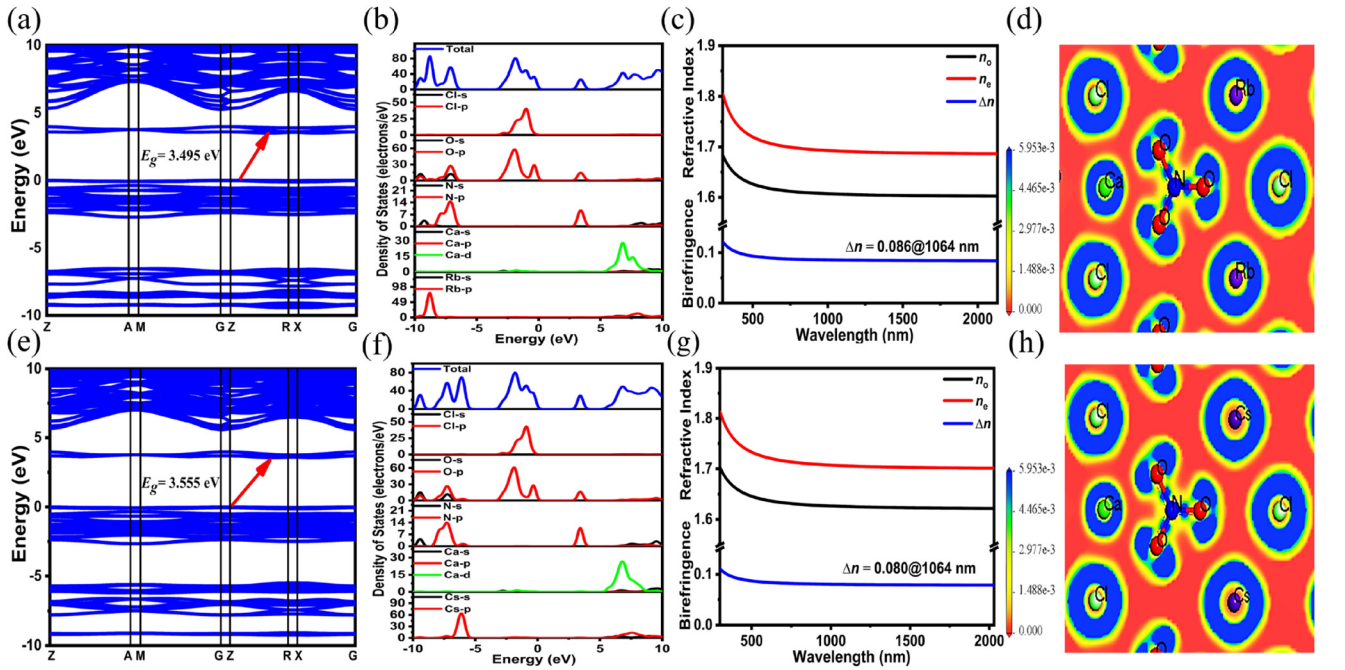

Fig. 5 Calculated band structures of $Rb_2Ca(NO_3)_2Cl_2$ and $Cs_2Ca(NO_3)_2Cl_2$ (a and e), DOS and PDOS of $Rb_2Ca(NO_3)_2Cl_2$ and $Cs_2Ca(NO_3)_2Cl_2$ (b and f), wavelength-dependent refractive indices for $Rb_2Ca(NO_3)_2Cl_2$ and $Cs_2Ca(NO_3)_2Cl_2$ (c and g), and electron localization functions of $Rb_2Ca(NO_3)_2Cl_2$ and $Cs_2Ca(NO_3)_2Cl_2$ (d and h).

the Fermi level, describe the optical properties of the material. Fig. 5b and f present the total and partial densities of states (DOS and PDOS) for $Rb_2Ca(NO_3)_2Cl_2$ and $Cs_2Ca(NO_3)_2Cl_2$. Near the Fermi level, O-2p and Cl-3p orbitals actively interact within the valence band. The conduction band is primarily formed from O-2p and N-2p states, indicating the presence of interactions consistent with N–O bonding characteristics. Based on the information presented, we can conclude that the linear optical properties of $Rb_2Ca(NO_3)_2Cl_2$ and $Cs_2Ca(NO_3)_2Cl_2$ are primarily the result of the interaction between the $[NO_3]$ groups and the CaO_4Cl_4 polyhedra.

It is widely recognized that the polarizability anisotropy of the $[NO_3]$ group is highest among the planar triangular anion groups, which also include $[BO_3]$ and $[CO_3]$.[49–51] Therefore, it can be inferred that the material may display significant birefringence when the $[NO_3]$ groups are arranged in a stacked manner, creating an ideal layered structure. The computed linear optical properties of $Rb_2Ca(NO_3)_2Cl_2$ and $Cs_2Ca(NO_3)_2Cl_2$ indicate that $n_z > n_x = n_y$, or equivalently, $n_e > n_o$, suggesting that these compounds are positive uniaxial optical crystals. The calculated birefringence values are 0.086@1064 nm for $Rb_2Ca(NO_3)_2Cl_2$ (Fig. 5c) and 0.080@1064 nm for $Cs_2Ca(NO_3)_2Cl_2$ (Fig. 5g), which are close to the experimental values. To illustrate the influence of different groups on birefringence, the techniques of electron localization function (ELF) and response electron distribution anisotropy[62] (REDA) are employed. ELF diagrams of $Rb_2Ca(NO_3)_2Cl_2$ and $Cs_2Ca(NO_3)_2Cl_2$ show a small impact of Ca^{2+} cations on the optical birefringence due to their almost spherical electron distribution, while the $[NO_3]$ units display distinct asymmetric lobes (Fig. 5d and h). The contributions from the $[Rb(1)O_6Cl_4]$, $[Ca(1)O_4Cl_4]$, and $[NO_3]$ groups in $Rb_2Ca(NO_3)_2Cl_2$ are calculated to be 4.99, 25.40, and 69.61 percent, respectively. Meanwhile, the contributions from the $[Cs(1)O_8Cl_4]$, $[Ca(1)O_4Cl_4]$, and $[NO_3]$ groups in $Cs_2Ca(NO_3)_2Cl_2$ are found to be 4.36, 22.78, and 72.86 percent, respectively, based on the calculated bonding electron density difference ($\Delta\rho$) values of the individual building units (Fig. S7a and b). This suggests that the $[NO_3]$ groups work together to enhance the anisotropy of the compounds, thereby affecting their birefringence values.

Conclusions

In conclusion, novel variants of layered Ruddlesden–Popper perovskites, $Rb_2Ca(NO_3)_2Cl_2$ and $Cs_2Ca(NO_3)_2Cl_2$, have been successfully synthesized for the first time by incorporating Ca^{2+} cations into the nitrate and chloride system. The integration of CaO_4Cl_4 polyhedra within a unique layered structure imparts tunable optical properties, including favourable short UV absorption edges (220–225 nm) and significant birefringence (0.099–0.104@546 nm). Title compounds also demonstrate high thermodynamic stability at temperatures ranging from 490 to 525 °C. Theoretical calculations indicate that the π-conjugated $[NO_3]$ anionic group significantly influences their optical anisotropy. This research not only expands the structural diversity of perovskite variants but also offers valuable

insights for the continued development of high-performance multifunctional optical materials, particularly in the UV region.

Author contributions

Fangfang Zhang supervised research and the manuscript revisions. Hussin Elkik designed and conducted the experiments, wrote the initial draft, and made revisions. Aqsa Munawar performed the theoretical calculations with assistance from Zhihua Yang. Muhammad Mujahid Iqbal contributed to the experimental work. Shilie Pan provided insights and guidance. All authors were involved in the discussions.

Conflicts of interest

The authors state that there are no conflicts of interest to disclose.

Data availability

The authors declare that the main data that support the findings of this study are available within the article and the supplementary information (SI). Other relevant data are available from the authors upon reasonable request.

Supplementary information: experimental related figures and tables. See DOI: **https://doi.org/10.1039/d6qi00086j**.

CCDC 2412905 (**1**) and 2412906 (**2**) contain the supplementary crystallographic data for this paper.[63a,b]

Acknowledgements

This work was supported by the Tianshan Innovation Team Foundation (2022TSYCTD0005), the Strategic Priority Research Program of the Chinese Academy of Sciences (XDB0880000) and the CAS Youth Interdisciplinary Team Foundation (JCTD-2022-19).

References

1 S. Niu, G. Joe, H. Zhao, Y. Zhou, T. Orvis, H. Huyan, J. Salman, K. Mahalingam, B. Urwin, J. Wu, Y. Liu, T. E. Tiwald, S. B. Cronin, B. M. Howe, M. Mecklenburg, R. Haiges, D. J. Singh, H. Wang, M. A. Kats and J. Ravichandran, Giant optical anisotropy in a quasi-one-dimensional crystal, *Nat. Photonics*, 2018, **12**, 392–396.

2 F. Zhang, X. Chen, M. Zhang, W. Jin, S. Han, Z. Yang and S. Pan, An Excellent Deep-Ultraviolet Birefringent Material Based on $[BO_2]_\infty$ Infinite Chains, *Light: Sci. Appl.*, 2022, **11**, 252–259.

3 F. Zhang, Z. Chen, C. Cui, Z. Yang, M. Mutailipu, F. Li, X. Hou, X. Long and S. Pan, A Full Breakthrough in Vacuum Ultraviolet Nonlinear Optical Performance of $NH_4B_4O_6F$, *Nature*, 2026, **650**, 97–101.

4 M. Arif, X. Liu, H. Jia, Z. Yang, X. Hou and S. Pan, Achieving Ultra-High Optical Anisotropy via Structural Regulation and Coplanar Engineering of Extended π-Conjugated $[H_{2(-x}C_3N_3S_3]$ (x = 1, 2) Groups, *Adv. Funct. Mater.*, 2026, **36**, e26914–e26922.

5 Y. Long, X. Dong, H. Zeng, Z. Lin and G. Zou, Layered Perovskite-like Nitrate $Cs_2Pb(NO_3)_2Br_2$ as a Multifunctional Optical Material, *Inorg. Chem.*, 2022, **61**, 4184–4192.

6 G. Ghosh, Dispersion-equation coefficients for the refractive index and birefringence of calcite and quartz crystals, *Opt. Commun.*, 1999, **163**, 95–102.

7 F. Sedlmeir, R. Zeltner, G. Leuchs and H. G. L. Schwefel, High-Q MgF_2 whispering gallery mode resonators for refractometric sensing in aqueous environment, *Opt. Express*, 2014, **22**, 30934–30942.

8 Z. Guoqing, X. Jun, C. Xingda, Z. Heyu, W. Siting, X. Ke, D. Peizhen and G. Fuxi, Growth and spectrum of a novel birefringent α-BaB_2O_4 crystal, *J. Cryst. Growth*, 1998, **191**, 517–519.

9 Y. Long, X. Dong, L. Huang, H. Zeng, Z. Lin and G. Zou, $CsHgNO_3Cl_2$: A New Nitrate UV Birefringent Material Exhibiting an Optimized Layered Structure, *Inorg. Chem.*, 2020, **59**, 12578–12585.

10 J. H. Wu, C. L. Hu, T. K. Jiang, J. G. Mao and F. Kong, Highly Birefringent d^0 Transition Metal Fluoroantimonite in the Mid Infrared Band: Order–Disorder Regulation by Cationic Size, *J. Am. Chem. Soc.*, 2023, **145**, 24416–24424.

11 J. Guo, A. Tudi, S. Han, Z. Yang and S. Pan, $Sn_2B_5O_9Cl$: A Material with Large Birefringence Enhancement Activated Prepared via Alkaline-Earth-Metal Substitution by Tin, *Angew. Chem., Int. Ed.*, 2019, **58**, 17675–17678.

12 J. Guo, J. Huang, A. Tudi, X. Hou, S. Han, Z. Yang and S. Pan, Birefringence Regulation by Clarifying the Relationship Between Stereochemically Active Lone Pairs and Optical Anisotropy in Tin-based Ternary Halides, *Angew. Chem., Int. Ed.*, 2023, **62**, e202304238–e202304242.

13 J. Guo, A. Tudi, S. Han, Z. Yang and S. Pan, Sn_2PO_4I: An Excellent Birefringent Material with Giant Optical Anisotropy in Non π-Conjugated Phosphate, *Angew. Chem., Int. Ed.*, 2021, **60**, 24901–24904.

14 S. Han, A. Tudi, W. Zhang, X. Hou, Z. Yang and S. Pan, Recent Development of Sn(II), Sb(III)-based Birefringent Material: Crystal Chemistry and Investigation of Birefringence, *Angew. Chem., Int. Ed.*, 2023, **62**, e202302025–e202302044.

15 A. Tudi, S. Han, Z. Yang and S. Pan, Potential Optical Functional Crystals with Large Birefringence: Recent Advances and Future Prospects, *Coord. Chem. Rev.*, 2022, **459**, 214380–214397.

16 H. Yu, N. Z. Koocher, J. M. Rondinelli and P. S. Halasyamani, Pb_2BO_3I: A Borate Iodide with the Largest Second-Harmonic Generation (SHG) Response in the $KBe_2BO_3F_2$ (KBBF) Family of Nonlinear Optical (NLO) Materials, *Angew. Chem., Int. Ed.*, 2018, **57**, 6100–6103.

17 S. D. Nguyen, J. Yeon, S. H. Kim and P. S. Halasyamani, $BiO(IO_3)$: A New Polar Iodate that Exhibits an Aurivillius-Type $(Bi_2O_2)^{2+}$ Layer and a Large SHG Response, *J. Am. Chem. Soc.*, 2011, **133**, 12422–12425.
18 C. Chen, Y. Wang, B. Wu, K. Wu, W. Zeng and L. Yu, Design and synthesis of an ultraviolet-transparent nonlinear optical crystal $Sr_2Be_2B_2O_7$, *Nature*, 1995, **373**, 1994–1996.
19 C. Chen, A. Jiang, B. Wu, G. You, S. Lin and Y. Wu, New nonlinear-optical crystal: LiB_3O_5, *Conf. Lasers Electro-Opt.*, 1989, **6**, 616–621.
20 Y. Wu, T. Sasaki, S. Nakai, A. Yokotani, H. Tang and C. Chen, CsB_3O_5: A new nonlinear optical crystal, *Appl. Phys. Lett.*, 1993, **62**, 2614–2615.
21 B. Wu, D. Tang, N. Ye and C. Chen, Linear and nonlinear optical properties of the $KBe_2BO_3F_2$ (KBBF) crystal, *Opt. Mater.*, 1996, **5**, 105–109.
22 T. T. Tran, J. He, J. M. Rondinelli and P. S. Halasyamani, $RbMgCO_3F$: A New Beryllium-Free Deep-Ultraviolet Nonlinear Optical Material, *J. Am. Chem. Soc.*, 2015, **137**, 10504–10507.
23 F. Kong, C. L. Hu, M. L. Liang and J. G. Mao, $Pb_4(OH)_4(BrO_3)_3(NO_3)$: An Example of SHG Crystal in Metal Bromates Containing π-Conjugated Planar Triangle, *Inorg. Chem.*, 2016, **55**, 948–955.
24 D. Lin, M. Luo, C. Lin, F. Xu and N. Ye, $KLi(HC_3N_3O_3)\cdot 2H_2O$: Solvent-drop Grinding Method Towards the Hydro-isocyanurate Nonlinear Optical Crystal, *J. Am. Chem. Soc.*, 2019, **141**, 3390–3394.
25 L. Qi, X. Jiang, K. Duanmu, C. Wu, Z. Lin, Z. Huang, M. G. Humphrey and C. Zhang, Quadruple-Bidentate Nitrate-Ligated $A_2Hg(NO_3)_4$ (A=K, Rb): Strong Second-Harmonic Generation and Sufficient Birefringence, *Angew. Chem., Int. Ed.*, 2023, **62**, 1–7.
26 Y. Zhang, Y. Long, X. Dong, L. Wang, L. Huang, H. Zeng, Z. Lin, X. Wang and G. Zou, $Y_8O(OH)_{15}(CO_3)_3Cl$: An Excellent Short-Wave UV Nonlinear Optical Material Exhibiting Infrequent Three-Dimensional Inorganic Cationic Framework, *Chem. Commun.*, 2019, **55**, 4538–4541.
27 P. S. Halasyamani and W. Zhang, ewpoint: Inorganic Materials for UV and Deep-UV NonlinearOptical Applications, *Inorg. Chem.*, 2017, **56**, 12077–12085.
28 H. Zhang, M. Zhang, S. Pan, Z. Yang, Z. Wang, Q. Bian, X. Hou, H. Yu, F. Zhang, K. Wu, F. Yang, Q. Peng, Z. Xu, K. B. Chang and K. R. Poeppelmeier, $Na_3Ba_2(B_3O_6)_2F$: Next Generation of Deep-Ultraviolet Birefringent Materials, *Cryst. Growth Des.*, 2015, **15**, 523–529.
29 Z. Jia, N. Zhang, Y. Ma, L. Zhao, M. Xia and R. Li, Top-Seeded Solution Growth and Optical Properties of Deep-UV Birefringent Crystal $Ba_2Ca(B_3O_6)_2$, *Cryst. Growth Des.*, 2017, **17**, 558–562.
30 A. J. Jacobson, J. W. Johnson and J. T. Lewandowski, Interlayer Chemistry between Thick Transition-Metal Oxide Layers: Synthesis and Intercalation Reactions of K $[Ca_2Na_{n-3}Nb_nO_{3n+1}]$ $(3 \leq n \leq 7)$, *Inorg. Chem.*, 1985, **24**, 3727–3729.
31 B. Zhao, D. Shen, Z. Zhang, P. Lu, M. Hossain, J. Li, B. Li and X. Duan, 2D Metallic Transition-Metal Dichalcogenides: Structures, Synthesis, Properties, and Applications, *Adv. Funct. Mater.*, 2021, **31**, 2105132–2105167.
32 X. Liu, P. Long, Z. Sun and Z. Yi, Optical, Electrical and Photoelectric Properties of Layered– perovskite Ferroelectric Bi_2WO_6 Crystals, *J. Mater. Chem. C*, 2016, **4**, 7563–7570.
33 S. Ghosh, B. Pradhan, Y. Zhang, D. Rana, D. Naumenko, H. Amenitsch, J. Hofkens and A. Materny, Investigation of Many-Body Exciton Recombination and Optical Anisotropy in Two-Dimensional Perovskites Having Different Layers with Alternating Cations in the Interlayer Space, *J. Phys. Chem. C*, 2021, **125**, 7799–7807.
34 Z. Wu, S. Li, Y. M. Yousry, W. P. D. Wong, X. Wang, T. Ma, Z. Chen, Y. Shao, W. H. Liew, K. Yao, F. Pan and K. P. Loh, Intercalation-driven ferroelectric-to-ferroelastic conversion in a layered hybrid perovskite crystal, *Nat. Commun.*, 2022, **13**, 1–8.
35 M. K. Kim, V. Jo and K. M. Ok, New Variant of Highly Symmetric Layered Perovskite with Coordinated NO_3^- Ligand: Hydrothermal Synthesis, Structure, and Characterization of $Cs_2PbCl_2(NO_3)_2$, *Inorg. Chem.*, 2009, **48**, 7368–7372.
36 *V. SAINT, Version 7.60 A*, Bruker Analytical X-ray Instruments, Inc., Madison, WI, 2008.
37 G. M. Sheldrick, A short history of SHELX, *Acta Crystallogr., Sect. A: Found. Crystallogr.*, 2008, **64**, 112–122.
38 A. L. Spek, Single-crystal structure validation with the program PLATON, *J. Appl. Crystallogr.*, 2003, **36**, 7–13.
39 J. Tauc, Absorption edge and internal electric fields in amorphous semiconductors, *Mater. Res. Bull.*, 1970, **5**, 721–729.
40 M. Arif, X. Liu, Z. Li, H. Jia, Y. Jiang, Z. Yang, X. Hou and S. Pan, Unveiling Charge Dependent Law to Enhance Birefringence in 2-Aminopyrimidine Family, *Adv. Opt. Mater.*, 2024, **13**, 2402327–2402337.
41 E. L. Simmons, Diffuse reflectance spectroscopy: a comparison of the theories, *Appl. Opt.*, 1975, **14**, 1380–1386.
42 S. Landi, I. R. Segundo, E. Freitas, M. Vasilevskiy, J. Carneiro and C. J. Tavares, Use and misuse of the Kubelka-Munk function to obtain the band gap energy from diffuse reflectance measurements, *Solid State Commun.*, 2022, **341**, 1–7.
43 L. Cao, G. Peng, W. Liao, T. Yan, X. Long and N. Ye, A Micro-crystals Method for the Measurement of Birefringence, *CrystEngComm*, 2020, **22**, 1956–1961.
44 S. J. Clark, M. D. Segall, C. J. Pickard, P. J. Hasnip, M. I. J. Probert, K. Refson and M. C. Payne, First principles methods using CASTEP, *Z. Kristallogr.*, 2005, **220**, 567–570.
45 K. Li, L. Luo, Y. Zhang, W. Li and Y. Hou, Generalized Gradient Approximation Made Simple, *ACS Appl. Mater. Interfaces*, 2018, **10**, 41525–41534.
46 J. D. Pack and H. J. Monkhorst, Special points for Brillonin-zone integrations, *Phys. Rev. B*, 1977, **16**, 1748–1749.

47 S. D. Griesemer, L. Ward and C. Wolverton, High-throughput crystal structure solution using prototypes, *Phys. Rev. Mater.*, 2021, **5**, 1–15.
48 H. Müller-Buschbaum and J. Wilkens, Ein Beitrag über Sr_2RuO_4 und $Sr_3Ru_2O_7$, Zur Oktaederstreckung von M^{4+} in K_2NiF_4- und $Sr_3Ti_2O_7$-Typ-Verbindunge, *Z. anorg. allg. Chem.*, 1990, **591**, 161–166.
49 X. Dong, L. Huang, Q. Liu, H. Zeng, Z. Lin, D. Xu and G. Zou, Perfect Balance Harmony in $Ba_2NO_3(OH)_3$: A Beryllium-Free Nitrate as UV Nonlinear Optical Material, *Chem. Commun.*, 2018, **54**, 5792–5795.
50 H. Zhou, M. Cheng, S. Pan and Z. Yang, La$(SO_3NH_2)_2NO_3{\cdot}H_2O$: Synergistic Anion Engineering of the First Rare-Earth Nitrate Sulfamate Defying Transparency-Birefringence-Nonlinearity Trade-Offs in Ultraviolet Nonlinear Optics, *Sci. China: Chem.*, 2025, DOI: 10.1007/s11426-025-2852-3.
51 L. Liu, Y. Yang, L. Li, Z. Yang and S. Pan, $SrNO_3(OH){\cdot}H_2O$: A New Member in Strontium Nitrate Hydrate Family with an Ultraviolet Cut-off Edge, *J. Alloys Compd.*, 2017, **695**, 1719–1724.
52 W. Zhang and P. S. Halasyamani, Crystal Growth and Optical Properties of a UV Nonlinear Optical Material $KSrCO_3F$, *CrystEngComm*, 2017, **19**, 4742–4748.
53 H. Hu, J. Huang, Z. Guo, M. Zhang, Z. Yang and S. Pan, $Ba_2B_5O_8(OH)_2(NO_3){\cdot}3H_2O$: the design of an alkaline earth metal borate-nitrate optimized from a hydroxylic borate, *Dalton Trans.*, 2022, **51**, 1979–1984.
54 Y. Song, C. Lin, X. Zhao, T. Yan, N. Ye, H. Tian and M. Luo, Synergistic combination of different types of functional motif in $Rb(NO_3)(SO_3NH_3)$ for realizing excellent ultraviolet optical nonlinearity, *Inorg. Chem. Front.*, 2024, **11**, 4329–4335.
55 X. Hao, C. Lin, M. Luo and N. Ye, $Sr(NH_2SO_3)(NO_3){\cdot}H_2O$: An Ultraviolet Nonlinear Optical Material Exhibiting Strong Second-Harmonic Generation Response and Sufficient Birefringence, *Inorg. Chem.*, 2023, **62**, 18020–18024.
56 Z. Zhang, D. Xu, Z. Wu, M. Hu, X. Su and Y. Huang, $KRb_2(NO_3)_2Cl$: a new birefringent crystal exhibiting a perovskite-related framework and a short cutoff edge, *Dalton Trans.*, 2023, **52**, 14303–14308.
57 W. Li, J. Wang, L. Liu, C. Huang, Y. Ding, M. M. Zhu, J. Tian, H. Qi, Y. Chu and J. Xu, $Na_3K_6(CO_3)_3(NO_3)_2X{\cdot}6H_2O$ (X = NO_3, Cl, Br): Exploring High Performance UV Birefringent Crystals Induced by Coplanar π-Conjugated CO_3 and NO_3 Groups, *Inorg. Chem.*, 2024, **63**, 8408–8417.
58 M. Zhang, D. An, C. Hu, X. Chen, Z. Yang and S. Pan, Rational Design via Synergistic Combination Leads to an Outstanding Deep-Ultraviolet Birefringent $Li_2Na_2B_2O_5$ Material with Unvalued B_2O_5 Functional Gene, *J. Am. Chem. Soc.*, 2019, **141**, 3258–3264.
59 A. Tkatchenko and M. Scheffler, Accurate Molecular van der Waals Interactions from Ground-State Electron Density and Free-Atom Reference Data, *Phys. Rev. Lett.*, 2009, **102**, 6–9.
60 A. J. Cohen, P. Mori-Sánchez and W. Yang, Fractional charge perspective on the band gap in density-functional theory, *Phys. Rev. B: Condens. Matter Mater. Phys.*, 2008, **77**, 1–6.
61 L. Wang, H. Wang, D. Zhang, D. Gao, J. Bi, L. Huang and G. Zou, Centrosymmetric RbSnF2NO3 vs. noncentrosymmetric $Rb_2SbF_3(NO_3)_2$, *Inorg. Chem. Front.*, 2021, **8**, 3317–3324.
62 J. Fan, Z. Yan, Z. Chen, H. Li, Z. Yang, F. Zhang and S. Pan, $Na_2B_6SO_{13}$ with unprecedented $[B_6SO_{13}]_\infty$ double chains and largest birefringence among borosulfates induced by the uniform arrangement of $[B_3O_7]$ units, *Sci. China: Chem.*, 2024, **68**, 475–480.
63 (*a*) CCDC 2412905: Experimental Crystal Structure Determination, 2026, DOI: 10.25505/fiz.icsd.cc2lztn2; (*b*) CCDC 2412906: Experimental Crystal Structure Determination, 2026, DOI: 10.25505/fiz.icsd.cc2lztp3.